Strain and Microcrystallite Size in Synthetic Lamellar Apatite

Adriyan S. Milev,* G. S. Kamali Kannangara, and Michael A. Wilson

College of Science, Technology and Environment, University of Western Sydney, Locked Bag 1797, Penrith South DC 1797, Australia

Received: March 24, 2004; In Final Form: June 3, 2004

Synthetic lamellar mixed A−B type carbonate containing apatite with two different Ca/P ratios (1.67 and 1.82) has been produced from a lamellar calcium acetate phosphonate precursor to investigate the impact of carbonate substitution on apatite crystal structure. Examination of X-ray diffraction line profile broadening was used to determine microcrystallite size and microstrain at different temperatures and to relate these to biological apatite. Both crystallite size and microstrain contributed considerably to the diffraction peak broadening in samples prepared below 700 °C. In the 500−700 °C temperature interval the crystallite sizes demonstrated a minimum at 600 °C, while a maximum for the microstrain was observed. The decrease of the crystallite size and the increase of the microstrain at 600 °C, were associated with structural arrangements in the phosphate sublattice. Above 700 °C, larger crystals are formed possessing little microstrain. It is shown that apatite formed at 600 °C with a Ca/P ratio of 1.82 is comparable in morphology, carbonate type, content, crystallite size, and microstrain to those in biogenic apatites. Infrared spectral analysis was used to quantify the carbonate type and content.

1. Introduction

Crystallization of biogenic apatite (Ap) is a complex process, which begins with heterogeneous nucleation of a calcium phosphate on an organic extracellular matrix.[1] Direct electron microscopy measurements and indirect X-ray diffraction techniques support the concept that bone crystals are all platelike particles with lengths and widths of 50 × 25 nm and thicknesses of 2−5 nm.[2] A lamellar precursor phase, octacalcium phosphate (OCP), is thought to act as a template for platelike apatite formation in vivo and in vitro.[3,4] During OCP → Ap biological transformation, carbonate ions may be incorporated into the apatite crystallites.[5] The carbonate ions are present in two different environments: (i) an environment involving substitution of CO_3^{2-} for OH (A- type apatite) and (ii) an environment involving substitution of CO_3^{2-} for PO_4^{3-} (B-type apatite).[6−9] The two types of substitution, A-type and B-type, can also occur simultaneously, resulting in a more complex, mixed A−B type substitution.[6,7] This combined mode of substitution has been found in bone and dental enamel.[8,9] However, the distribution between type A and B sites has not been established precisely, though it has been realistically assumed that type B carbonate is the major species.[9,10,21]

The presence of carbonate and other ionic substitutions in biogenic apatites was related to change in the unit cell parameters, the crystal morphology, limitations in crystallite size, and the presence of strain and/or distortion resulting from dislocations and vacancies.[11−15] Stokes and Wilson[16] described this strain, termed microstrain, as a change in the *d*-spacing in a strained sample compared with an unstrained one. Two types of strains have been recognized, uniform and nonuniform strain. There is no broadening related to uniform strain, whereas nonuniform strain leads to systematic shifts of the atoms from their ideal positions and to broadening of the diffraction lines. The nonuniform broadening arises from the following sources: (i) vacancies or site disorder, (ii) poor crystallinity, and (iii) plastic deformations.[16,17] The strain (STR) is a dimensionless parameter usually expressed as a root-mean-square strain ($\langle e^2_{RMS}\rangle^{1/2}$).[18] The crystal size and microstrain have important roles in the osteogenic process, because these factors influence the solubility and bioactivity properties of the biological apatites.[19−23] In attempts to prepare biological material under laboratory conditions, it is necessary therefore to incorporate carbonate in both A and B positions and in similar proportions to the particular biological material being mimicked. It is also necessary to imitate apatite morphology, crystallite size, and microstrain since the bone osteoblast cells are sensitive not only to the chemical composition but also to the physical properties of their immediate surroundings. These properties include surface composition, surface energy, roughness, and topography.[24,25]

Klug and Alexander[26] reported that both microstrain and crystallite size values can be obtained by a more detailed analysis of diffraction line broadening by different analytical procedures (Fourier, integral breadth (IB), and single line analysis). The deconvolution Fourier procedure does not a priori assume a shape function, but the method is susceptible to error due to peak overlap. The second approach, the integral breadth (peak area divided by peak height) methods exploit the different angular dependencies of crystal size and strain-induced broadenings. The crystallite size broadening is generally considered independent of the order of reflections (e.g., 001, 002, 004, etc.), whereas the effect of microstrain depends on two theta (2θ) and therefore on the order of reflection.[17,26,27] This is the basis of their separation. However, the Fourier and integral breadth approaches are differently defined and therefore not necessarily comparable. The RMS values obtained from the Fourier and integral breadth approaches can be compared only in the case of Gaussian strain distribution.[26−29] Both integral breadth and

* Corresponding author. College of Science, Technology and Environment, University of Western Sydney, Building LZ, Parramatta Campus, Locked Bag 1797, Penrith South DC 1797, Australia. Tel.: +61 2 9685 9936. Fax: +61 2 9685 9915. E-mail address: a.milev@uws.edu.au.

10.1021/jp048677m CCC: $27.50
Published on Web 08/04/2004

Fourier methods gain in reliability when more than one order of reflection is used.[28] When multiple reflections are not available, single-line analysis based on a Voigt function allows determination of the crystallite size and microstrain simultaneously.[29,30] All methods for size/strain analysis require knowledge about the instrumental contribution to the peak broadenings. This is usually obtained by using standards that are highly crystalline and possess no microstrain, such as Si or LaB_6. Then, the instrumental broadening is subtracted from the sample broadening.

Recently, a peak-fitting method called the Fundamental Parameters (FP) approach for more accurate line profile analysis has been proposed.[31,32] It has been known for quite some time[33] but it has only lately been implemented as a standard fitting procedure.[34] FP method allows for a precise determination of the profile shape, correction of the peak positions, peak intensity or integrated intensity, and refining of line widths. It employs the integral breadth method for crystalline size and strain analysis. The size/strain analysis can be carried out with higher accuracy than the existing methods because it does not require knowledge about the instrumental contribution to the line broadening. The synthesized-by-FP profile rather than a profile from a reference material is used to deconvolute the instrumental effects from the observed profiles. The synthesis of peak profiles is based on convolution of the (i) spectral distribution of the X-ray source (tube), (ii) geometry and the configuration of the diffractometer, and (iii) microstructural factors of the samples (crystallite size and microstrain effects).[35] This method is used here.

In our previous reported studies, we have been successful in mimicking apatite morphology.[36,37] However, to our knowledge there have been no reports of mimicking microstrain, crystallite size, and particle morphology. Here we use a modified method for synthesis of apatite with similarities in morphology and carbonate substitution.[36−38] The purpose of the present work was to extract crystallite size and microstrain parameters separately for synthetic lamellar apatite with two different Ca/P ratios. The crystallite size and microstrain were determined simultaneously by total pattern fitting in the 2θ region of 24−55 deg. Average crystal size/perfection (crystallinity) determined from X-ray diffraction by the FP approach is correlated with parameters derived from the corresponding IR spectra and the Ca/P ratio. These findings are compared with crystallite sizes and microstrain data of biogenic apatites reported in the literature.

2. Materials and Methods

Sample Preparation. Details of the preparation of hydroxyapatite from a phosphonate precursor and the reaction mechanisms in solution are reported elsewhere.[37] However, the calcium and phosphorus source compounds have been changed. In this work, calcium acetate half-hydrate [$Ca(CH_3COO)_2 \cdot 0.5H_2O$] and dimethyl hydrogen phosphonate [$HP(O)(CH_3O)_2$] were used at Ca/P ratios of 1.67, 1.82, and 2.0. The latter two were prepared calcium-rich to study the impact of carbonate inclusions on the apatite lattice. The dimethyl hydrogen phosphonate amount (Sigma, >98% purity) was changed to obtain Ca/P ratios of 1.67, 1.82, and 2.0. (3.400×10^{-3}, 3.119×10^{-3}, and 2.839×10^{-3} mol, respectively) while maintaining a constant weight (1.000 g) of calcium acetate half-hydrate (Aldrich, >99% purity) in all samples. The calcium and phosphorus precursors were dissolved in a mixed solvent prepared from ethylene glycol (Fluka, >99.5% purity) and acetic acid (Sigma, >99.7% purity) in 1:1 molar ratio (0.08 mol of each). The mixtures were stirred for at least 30 min at ambient temperature to dissolve the calcium acetate precursor and then were heated at 70 °C for 48 h in closed vials. The ^{31}P nuclear magnetic spectral data for the solution showed that this modified synthetic procedure resulted in a higher yield (about 80% vs ~71% in the previous reported procedure) of acetyl 2-hydroxyethyl phosphonate. The reaction products were dried at 130 °C for 48 h, and then decomposed at 300 °C for 24 h in air. The material was then fired in air at 500, 600, 700, 800, and 900 °C at a heating rate of 10 °C/min followed by a dwell period of 2 h at the respective temperature.

Analytical Methods. A Leo Supra 55VP scanning electron microscope (SEM) at 5 kV and a Philips Biofilter 120 operated at 120 kV transmission electron microscope (TEM) were used for imaging. For TEM investigations the specimens were sonicated in ethanol to separate aggregates. A drop of the apatite suspension is transferred onto lacey carbon foils supported on copper grids for final examination.

Carbonate Content. Infrared spectra of the solid products were obtained using KBr disks (≈1 mg sample suspended in about 150 mg KBr, 256 scans at 2 cm^{-1} resolution) using a Nicolet Magna 560 FT−IR spectrometer. The analysis chamber was continuously purged during the scanning with a current of decarbonated dry air. The carbonate content was estimated by an IR method that uses normalized extinctions (E) of the carbonate band near 1415 cm^{-1} and the phosphate band near 575 cm^{-1}, as described elsewhere.[39] The extinctions were calculated from measurements of baseline transmittance (T_b) and peak transmittance (T_p) using the relationship

$$E = \log(T_b/T_p) \tag{1}$$

The procedure involved mixing of synthetic apatite with calcium carbonate in proportions that were found in biogenic apatites (1−12 wt %). The extinction ratios were plotted against the particular carbonate content of the samples. Linear regression was carried out for the results, and gave a straight-line fit with a correlation coefficient 0.998:

$$\%CO_3^{2-} = 16.1(E_{1415}/E_{575}) - 0.2 \tag{2}$$

Eq 1 and eq 2 were used to estimate the carbonate content of the samples produced in the present work. The spectra were baseline corrected near the respective carbonate and phosphate vibration domains employing Grams/32 Spectral Notebase software Version 4.01 (Galactic Industries, Salem, NH). The T_b and T_p values were measured at the respective wavenumbers and the carbonate contents were determined according to eq 2. The A-to-B and L-to-B type carbonate ratios were compared on the basis of the respective A (880 cm^{-1}), B (873 cm^{-1}), and L (866 cm^{-1}) extinction ratios in a ν_2 carbonate domain determined via eq 1 (Table 1). The data were derived from the respective infrared spectra in transmission terms.

Profile Fitting. Diffraction patterns were collected on a Philips PW1825/20 diffractometer with a 173 mm goniometer radius, employing a Cu X-ray tube (40 kV, 30 mA), as well as incident and diffracted beam Soller slits with 5.1° acceptance angles. The diffraction patterns were collected over the 2θ range of 8−80° with an acquisition time of 10.0 s at a 0.02° step size. The XRD pattern profiles and precise peak positions were determined using the Fundamental Parameters approach, which employs the XFIT program.[31]

Line Broadening. The relatively well-developed apatite peaks in the 2θ range of 24−55° were used to derive information about the crystallite size and microstrain. The emission profile lines

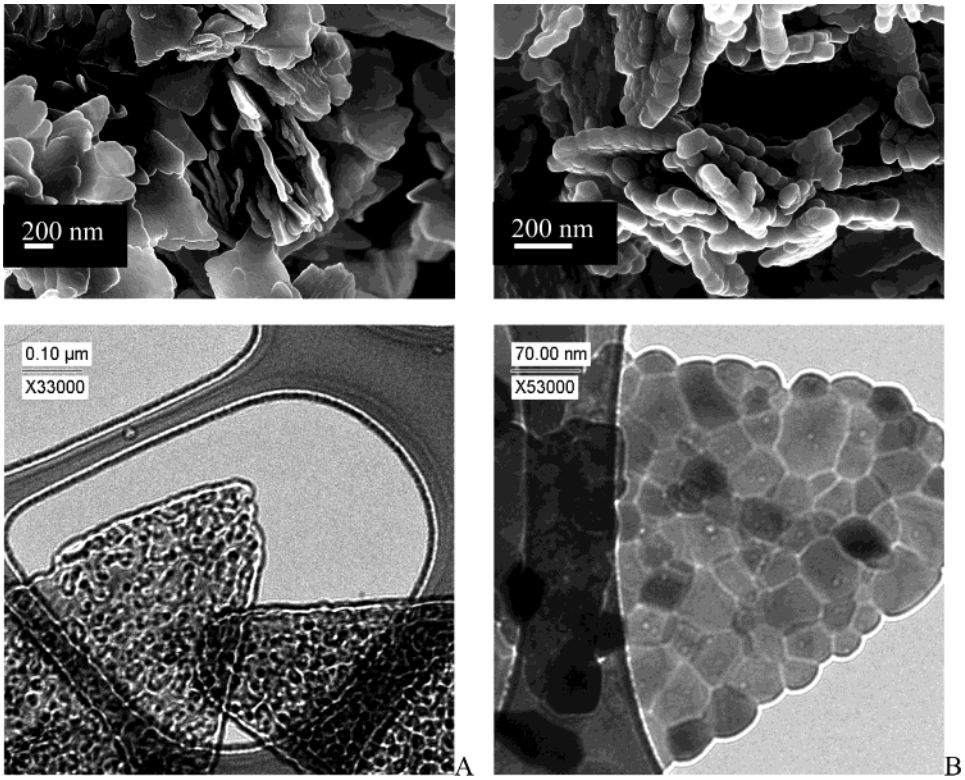

Figure 1. SEM (top) and TEM (bottom) micrographs of hydroxyapatite powders (Ca/P 1.67) obtained at A (500 °C) and B (900 °C) for 2 h at a 10 °C/min heating rate. TEM micrographs show individual platelets while SEM shows stacked sheets. Recrystallization within an individual platelet can be observed at 900 °C.

TABLE 1: Estimation of Carbonate Type and Amounts in Thermally Transformed Phosphonates into Apatite. A/B- and L/B-Type Extinction Ratios Corresponding to the Carbonate Ratios Are Given. Note that the Extinction Ratios Can Be Used Only as Estimation and Absolute A-to-B or L-to-B Carbonate Ratios Cannot Be Derived

	Ca/P = 1.67			Ca/P = 1.82		
temp. (°C)	%CO_3	E_A/E_B	E_L/E_B	%CO_3	E_A/E_B	E_L/E_B
900	1.0	0.61	-	1.4	0.72	-
800	1.2	0.49	-	2.4	0.46	-
700	1.4	0.55	0.27	3.3	0.54	0.26
600	2.3	1.28	0.76	6.9	0.55	0.48
500	5.3	0.83	0.83	9.7	0.66	0.64

for Cu Kα and K$_\beta$ were numerically convoluted with a Gaussian function to represent strain broadening and a Lorentzian to represent crystallite size broadening.[31,32] The line broadening due to the crystallite size as implemented in XFIT is represented by the well-known Debye−Scherrer formula $fwhm = \lambda/(D_v \cos\theta)$. The volume-weighted domain size (D_v) (denoted as crystallite size) is related to crystal sizes (nm), the line broadening as Full Width at Half Maximum (*fwhm*) in radian is described by a Lorentzian fit (λ is the wavelength, θ in radians). For the Gaussian peak shape, *fwhm* and *IB* can be given as $IB = [\pi/(4 \ln 2)]^{1/2}$ *fwhm*. The strain data obtained by XFIT are presented in the form of percentage of root-mean-square ($\langle e^2_{RMS}\rangle^{1/2}$) strain, which is related to *STR* via $\langle e^2_{RMS}\rangle^{1/2} = (2/\pi)^{1/2}$ STR. The line broadening measured as integral breadth due to the lattice strain can be expressed as $IB = 4\ STR \tan\theta$. Therefore, the relationship between the line broadening and percentage microstrain is $fwhm = 4(2 \ln(2))^{1/2} \tan\theta\ STR/100$.[31]

A silicon standard similar to that described in "Standard Reference Material" SRM 640c by the National Institute of the Standards and Technology (NIST) was used to test the FP convolution algorithm and the diffractometer setup. A very good agreement between the predicted and the measured profiles was obtained.

Lattice Parameters. The correct peak positions in the 2θ interval 8−80° were determined via the FP approach. They were used as input data for unit cell determination. The input data were (*hkl*) indices, 2θ positions, tolerance of measurement, crystal system, and X-ray source. The values of the lattice constants were obtained by least-squares refinement of a hexagonal unit cell by employing CELREF 2 unit cell refinement software.[40] The refinements were based on the JCPDS standard, File Card No. 9-432, with *a*-axis = 0.94180 nm and *c*-axis = 0.68840 nm, and space group $P6_3/m$. Between 12 and 30 reflections were used to refine unit cell parameters.

3. Results and Discussion

3.1 Electron Micrographs. For clarity, electron micrographs of samples prepared in this work are briefly described. Figure 1 shows typical SEM and TEM micrographs of hydroxyapatite particles. The SEM shows apatites lamellae stacked together that form the apatite particles (Figure 1A), while the TEM micrograph shows a delaminated very thin apatite lamella deposited on lacey carbon support films. The stacked lamellae have a total thickness of about 80−100 nm. The most important observation is that the apatite particle thickness is similar to the thickness of the phosphonate precursor, which may be controlled by the number of deposited calcium phosphonate layers. Above 700 °C the lamellae sinter and the template effect of the phosphonate precursor is lost. The typical hexagonal habitus of the highly crystalline apatite particles can easily be observed at 900 °C (Figure 1B). Therefore, the expected benefit of the apatite particles morphology on the osteointegration process is likely at relatively low temperatures.

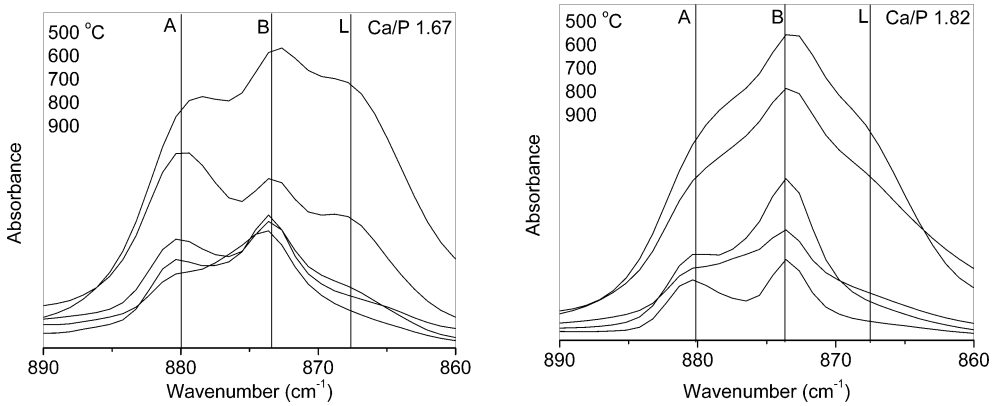

Figure 2. FT−IR spectra of CO_3^{2-} in the ν_2 (890−860 cm^{-1}) domain with two Ca/P ratios: *A* (Ca/P 1.67) and *B* (Ca/P 1.82).

3.2 Carbonate Inclusion. A model recently proposed by Gibson and Bonfield[7] suggests how apatite can be substituted with several percent carbonate occupying two different lattice positions (mixed A−B type).[41] The mechanism can be described as $Ca_{10}[(PO_4)_{6-x}(CO_3)_x][(OH)_{2-x}(CO_3)_x]$. This model does not require reduction of the number of calcium ions and monovalent cation incorporation to maintain the charge balance, if equimolar substitution at A and B-sites occurs simultaneously. The mechanism was used as a working formula when the starting solutions were prepared. If $x = 1$, the net reaction involves substitution of two moles of carbonate with one mole of phosphate and one mole of hydroxide ion to result in a mixed A−B type apatite. In that case, the Ca/(P + C) ratio is 1.67 (C is the number of moles of carbonate at B site) but Ca/P is 2.0. The theoretical carbonate content is then 11.8 wt %. However, the material with a Ca/P ratio of 2.0 did not result in a single-phase apatite. At lower temperatures (up to about 600 °C) it contained a $CaCO_3$ phase, which at higher temperatures (>700 °C) was converted to CaO. When $x = 0.5$, the Ca/P ratio is 1.82; this apatite was a single phase up to about 700 °C. According to the mechanism above, the total carbonate content is 5.9 wt %. Thus, the apatite molecule must have about 3 wt % carbonate groups at the B-site and the same amount at the A-site. Any deviation from these amounts would lead to charge imbalances and nonstoichiometry.

To quantify the results from X-ray line broadening analysis, information about carbonate type and amounts was required. The carbonate content was calculated based on a previously reported internal standardization method[39] exploiting IR ν_3 carbonate and ν_4 phosphate bands ratios.[42] Table 1 shows that the total carbonate content decreased with the temperature increase. Although the apatite with a Ca/P ratio of 1.67 contains some carbonate, it was much less compared to the apatite with a Ca/P ratio of 1.82 at 500 °C (9.7 vs 5.3 wt %). The FT−IR analysis provided information on the sites from which the carbonate was lost during heating. The intensity of the carbonate vibrations decreased significantly above 700 °C with emergence of CaO for the samples with a Ca/P ratio of 1.82. Some of the CaO reacted with atmospheric moisture, giving rise to the $Ca(OH)_2$ phase. It was detected by IR as a new OH band at 3644 cm^{-1} (not shown here). The IR also showed that above 700 °C peaks corresponding to lattice OH groups at about 3570 (OH stretch) and 633 cm^{-1} (OH libration) appeared. The presence of these bands indicated that some of the A-type carbonate was substituted by OH groups during heating.

The ν_2 carbonate domain consisted of three bands indicative of the type of carbonate present (Figure 2). The positions of these bands have been reported in the literature.[8,9,43,44] The carbonate groups located at the hydroxyl give rise to the band at about 880 cm^{-1}, whereas carbonate groups located at phosphate sites show resonances near 873 cm^{-1}. The presence of a third type carbonate species was detected at about 866 cm^{-1}, which was attributed to labile carbonate (L).[8] It has been suggested that L-type carbonate is not associated with the apatite structure; rather, it represents carbonate species in an amorphous environment or absorbed on different faces of the apatite lattice.[8,9,45,46] This carbonate type was nearly lost above 700 °C. Rey et al.,[8,9] indicated that a direct comparison of the peak intensities in the ν_2 carbonate domain may lead to a deceptive conclusion for the real A-to-B apatite ratio. Equivalent intensities of the bands at 880 and 873 cm^{-1} may correspond to a 2.5−3 times higher amount of B-type carbonate.[47] This means that there was more B-type carbonate than A-type at any temperature, though the $E_A > E_B$ at 600 °C for the samples with Ca/P of 1.67 (Table 1). The apatite with Ca/P 1.82 demonstrated generally higher extinctions corresponding to B-type than to A-type carbonate and smoother changes with increasing temperature. Above 700 °C the samples with either Ca/P ratios exhibited similar relative carbonate ratios and total carbonate contents.

3.3 X-ray Analysis. The carbonate substitutions in apatites are known to change the crystal lattice parameters. They depend on the type of substitution; pure type A (CO_3^{2-} for OH^-) causes expansion of the *a*- and the contraction of the *c*-axis parameters.[6] In contrast, pure type-B carbonated apatite (CO_3^{2-} for PO_4^{3-}) causes contraction of the *a*- and expansion of the *c*-axis dimensions.[48,49] Because of axial divergence and other instrumental factors, there can be a considerable asymmetry of the line profile and peak positions, especially at the low-angle region. The distorted line profiles and shifted peak positions can also contribute to poor resolution of the X-ray pattern. The effect of carbonate ion substitutions on the apatite peak positions were determined by employing FP approach. The precisely determined peak positions were used to calculate the unit cell parameters as a function of temperature. Less precise data were derived for the apatite with a Ca/P ratio of 1.82 prepared at 600 °C because only 12 reflections were useful due to the significant broadening. Figure 3 shows the change of the *a*- and *c*-lattice parameters of samples as a function of temperature. The *a*-parameter values for the samples with a Ca/P ratio of 1.67 indicated the highest amount of A-type carbonate in the 500−600 °C interval (Figure 3 and Table 2) while the lower than stoichiometric apatite values of the *a*-axis parameter (above 700 °C) showed that some of carbonate groups substitute for phosphate. In contrast, the lower value of the *a*-axis parameter and higher value of the *c*-axis parameter at 500 °C for the sample

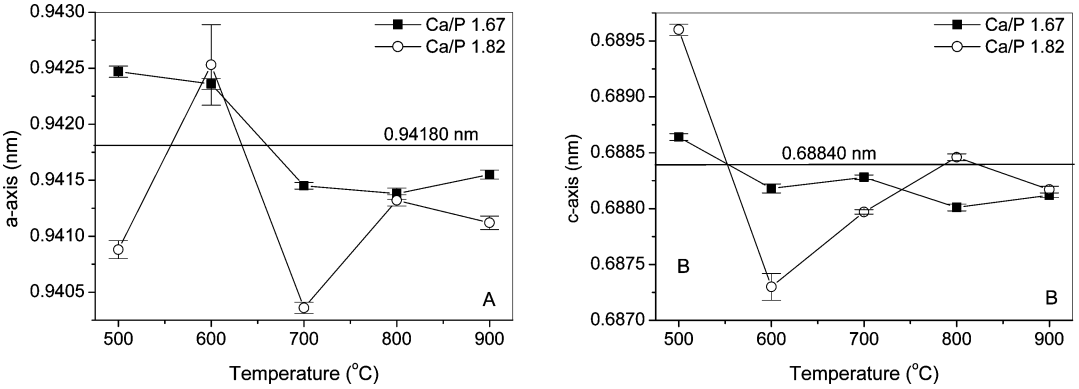

Figure 3. Variation of *a*- (A) and *c*-axis (B) lattice parameters as a function of temperature. The parameters were determined from least-squares analysis of peaks after FP refining. Error bars were derived from the least-squares fit of more than 30 diffraction maxima. The sample with a Ca/P ratio of 1.82 fired at 600 °C showed fewer peaks that could be reliably fit to the analytical profiles.

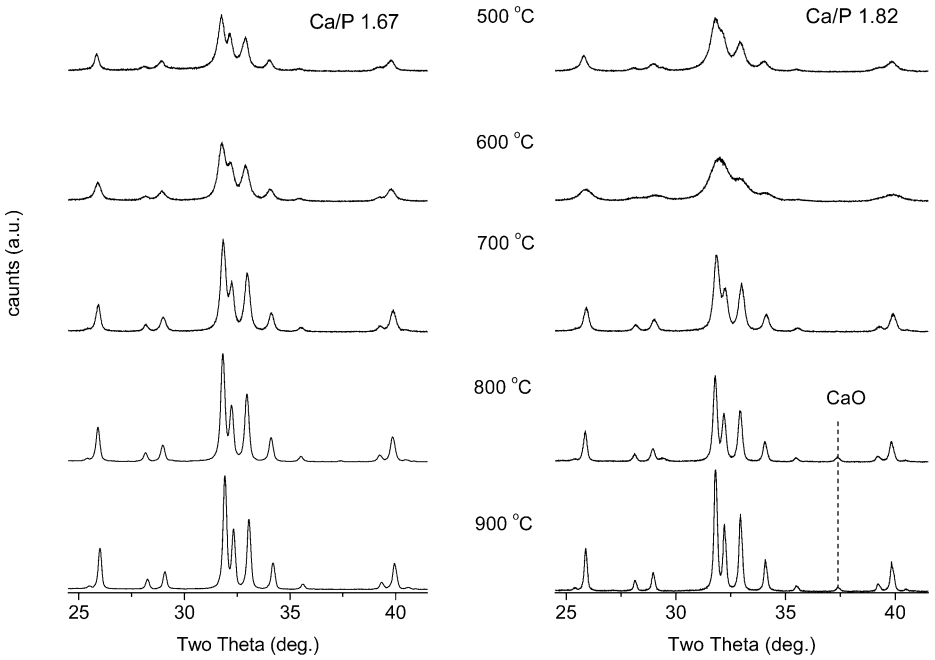

Figure 4. X-ray powder diffraction patterns of two series of apatite samples (Ca/P 1.67 and Ca/P 1.82) fired in the temperature interval 500−900 °C for 2 h. A diffraction peak at 37.5° corresponding to CaO is observed for samples with a Ca/P ratio of 1.82 above 700 °C.

TABLE 2: Refined *c*- and *a*-axis Parameters of Hap with Ca/P Ratios of 1.67 and 1.82 and the Respective Standard Errors (σ)

T (°C)	Ca/P 1.67				Ca/P 1.82			
param.	*a* (nm)	σ	*c* (nm)	σ	*a* (nm)	σ	*c* (nm)	σ
900	0.94155	0.00004	0.68812	0.00002	0.94112	0.00006	0.68817	0.00003
800	0.94138	0.00005	0.68801	0.00003	0.94132	0.00005	0.68846	0.00003
700	0.94145	0.00003	0.68828	0.00002	0.94036	0.00005	0.68797	0.00002
600	0.94236	0.00005	0.68818	0.00004	0.94253	0.00036	0.68730	0.00012
500	0.94247	0.00005	0.68864	0.00003	0.94088	0.00008	0.68960	0.00005

with a Ca/P ratio of 1.82 revealed much more of B- than A-type carbonate. The *c*-axis parameter decreased considerably at 600 °C and then steadily increased, reaching values closer to stoichiometric apatite at 800 °C. The *a*-axis parameter followed a reverse trend with a maximum at 600 °C and a minimum at 700 °C, thereafter it steadily attained values closer to those of stoichiometric apatite. Increasing the temperatures above 700 °C resulted in partial decomposition of the apatite with a Ca/P ratio of 1.82. The decomposition was accompanied with the appearance of a diffraction peak corresponding to CaO (Figure 4). The development of the CaO phase may be attributed to the loss of carbonate groups as carbon dioxide from the phosphate sublattice, thus increasing the Ca/(P + C) ratio. As previously reported, a significant change in carbonate content and crystallinity occurs in this temperature region.[38] The lattice parameters supported the IR data that carbonate substitutions are mixed A−B type for both Ca/P ratios.

Carbonate substitutions create vacancies and distortions in the apatite lattice that may result in increased microstrain. Our preliminary work on individual peak fitting showed a major difference in peak broadenings (*fwhm*) of (002) and (004) reflections at 500−700 °C. Above 700 °C, however, the *fwhm* values for these two reflections were very close. This means that the observed broadenings were partly due to crystallite size and partly due to lattice distortions. Therefore, a more rigorous approach than single line broadening analysis was needed. Line profile analysis via the FP approach in the 2θ region of 24−55° produced quantitative estimates of the average crystallite

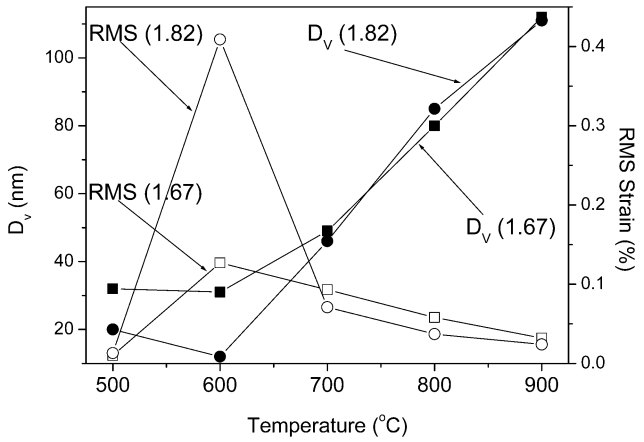

Figure 5. Size and microstrain changes as a function of temperature and Ca/P ratio. Open symbols correspond to microstrain. The obtained values of the crystallite size and the microstrain are averaged for all crystallographic directions.

size and RMS for all samples (Figure 5). Interestingly, at 600 °C the XRD lines were broader than those at 500 °C with contributions from both size and microstrain (Figure 4). This effect was more evident for the sample with a Ca/P ratio of 1.82, which demonstrated two times smaller crystallites and three times larger microstrain than the samples with a Ca/P ratio of 1.67 at 600 °C. Above 700 °C the lattice microstrain significantly decreased and crystal growth led to relatively large crystals of about 110 nm at 900 °C. The values of the crystallite size and microstrain in the interval 500−700 °C (up to 0.4%) are comparable to those in human enamel (0.1%),[19] human cortical bone (0.6%),[50,51] and calcified turkey leg tendon (0.3%).[52,53]

X-ray analysis showed that apatite with a Ca/P ratio of 1.82 underwent drastic constitutional changes upon heating. Infrared data indicated that the amount of A-type carbonate was much less than the amount of B-type carbonate at any temperature for both Ca/P ratios. The carbonate content at 500 °C was 9.7 wt %, which decreased upon heating to 6.9 wt % at 600 °C. At 700 °C, it decreased to a total of 3.3 wt % carbonate, which was not sufficient to maintain the Ca/(P + C) ratio of 1.67. The reduction of the carbonate content was accompanied with high microstrain. The microstrain lessens with the development of the separate CaO phase, which allowed restoration of the apatite stoichiometry with much less carbonate content. Therefore, the cause of the high microstrain observed for the sample with a Ca/P ratio of 1.82 at 600 °C was the structural rearrangements in the phosphate sublattice. The increase of the *a*-axis parameter at 600 °C indicated that the decomposition of B-type carbonate may proceed through temporary occupation of the A-site before leaving the apatite lattice as CO_2. In this case, the crystal lattice expands and the *a*-parameter increases primarily because of the rearrangements of the apatite lattice with phosphate groups. It seems, therefore, that the lattice parameters follow the exclusion of the carbonate ions.

In summary, IR and XRD data show that the synthetic platelike apatite with a Ca/P ratio of 1.82 can be considered as a mixed A−B type carbonate with a greater concentration of B -type than A-type. The data also suggested that the high carbonate content made the apatite lattice more defective and less stable. The appearance of OH vibrations at and above 700 °C for either Ca/P ratios indicated that a different charge compensation mechanism that includes incorporation of OH groups is more probable than the one given above. Such a mechanism may also involve formation of cationic or anionic vacancies in the apatite lattice.

The values for the crystallite size and microstrain reported here were based on the inherent broadening effect by the apatite crystals obtained from the pattern fitting in the 2θ region of 24−55° via the FP approach. It means that all relative well-developed apatite peaks were included in the evaluation procedure. Because these peaks include different *hkl* indices, the results relate to some kind of average for all crystallographic directions. As described above, the rationale for the platelike morphology, carbonate substitution, crystallite sizes, and microstrain was to produce a synthetic apatite with chemical and morphological attributes closer to that of bone mineral and thereby enhancing biological integration. The function of carbonate ions in the enhanced dissolution tendency of carbonated apatite may be explained, on the basis of its destabilizing effects on apatites, by the formation of defects in the crystals. When heated to $T > 700$ °C, the small highly strained crystals became significantly larger with little microstrain. Hence, the smaller surface area and reduced microstrain may significantly decrease the bioactivity of the material.

4. Conclusions

(1) Line profile XRD analysis produced quantitative estimates of the crystalline size and microstrain in apatites produced at different temperatures from calcium acetate and dimethyl hydrogen phosphonate as starting materials in 1.67 and 1.82 Ca/P ratios. The values of the crystallite size and microstrain in the interval 500−700 °C (up to 0.4%) are comparable to those in human enamel (0.1%), human cortical bone (0.6%), and calcified turkey leg tendon (0.3%).

(2) FT−IR and XRD data show that reduction in the carbonate content of the series of apatites is accompanied with high strain due to loss of stoichiometry. It is suggested that the decomposition of B-type carbonate in the lattice as the apatite releases a second phase of CaO proceeds through temporary occupation of the A-site.

Acknowledgment. This work was supported by UWS internal grant # 20711−80507 and the ARC Centre for Functional Nanomaterials.

References and Notes

(1) Mann, S. *Nature* **1993**, *356*, 499.
(2) Robinson, A. *J. Bone Joint Surg.* **1952**, *34A*, 389.
(3) Brown, W. *Nature* **1962**, *196*, 1048.
(4) Brown, W.; Schroeder, L.; Ferris, J. *J. Phys. Chem.* **1979**, *83*, 1385.
(5) Chicherur, N.; Tung, M.; Brown, W. *Calcif. Tissue. Int.* **1980**, *32*, 55.
(6) DeMaeyer, E.; Verbeeck, R.; Nassens, D. *Inorg. Chem.* **1993**, *32*, 5709.
(7) Gibson, I.; Bonfield, W. *J. Biomed. Mater. Res.* **2002**, *59*, 697.
(8) Rey, C.; Ranugopalakrishnan, V.; Collins, B.; Glimcher, M. *Calcif. Tissue Int.* **1991**, *49*, 251.
(9) Rey, C.; Collins, B.; Goehl, T.; Dickson, I.; Glimcher, M. *Calcif. Tissue Int.* **1989**, *45*, 157.
(10) LeGeros, R. *J. Dent. Res.* **1990**, *69*, 567.
(11) LeGeros, R. *Nature* **1965**, *206*, 403.
(12) LeGeros, R.; Trautz, O.; LeGeros, J.; Klein, E. *Science* **1967**, *155*, 1409.
(13) Nelson, D. *J. Dent. Res.* **1981**, *60*, 1621.
(14) Nelson, D.; Featherstone, J.; Duncan, J.; Cutress, T, *Caries Res.* **1983**, *17*, 200.
(15) Baig, A.; Fox, J.; Hsu, J.; Wang, Z.; Otsuka, M.; Higuchi, W.; LeGeros, R. *J. Colloid Interface Sci.* **1996**, *179*, 608.
(16) Stockes, A.; Wilson, A. *Proc. Phys. Soc., London* **1944**, *56*, 174.
(17) Langford, J.; Delhez, R.; Keijser, T.; Mittemeijer, E. *Aust. J. Phys.* **1988**, *41*, 173.
(18) Warren, B. *X-ray Diffraction*; Addison-Wesley: MA 1969.

(19) Baig, A.; Fox, J.; Young, R.; Wang, Z.; Hsu, J.; Higuchi, W.; Chhettry, A.; Zhuang, H.; Otsuka, M. *Calcif. Tissue Int.* **1999**, *64*, 437.
(20) Bonar, L.; Roufosse, A.; Sabine, W., Grynpas, M.; Glimcher, M. *Calcif. Tissue Int.* **1983**, *35*, 202.
(21) Fisher, L.; Eanes, E.; Denholm, L.; Heywood, B.; Termine, J. *Calcif. Tissue Int.* **1987**, *40*, 282.
(22) LeGeros, R.; Tung, M. *Caries. Res.* **1983**, *17*, 419.
(23) Okazaki, M.; Noriwaki, Y.; Aoba, T.; Doi, Y.; Takahashi, J. *Caries Res.* **1981**, *15*, 477.
(24) Elliott, J. *Structure and Chemistry of the Apatites and Other Calcium Orthophosphates*; Elsevier: London, 1994.
(25) Shwartz, Z.; Lohmann, C.; Oefinger, J.; Bonewald, L.; Dean, D.; Boyan, B. *Adv. Dent. Res*. **1999**, *13*, 38.
(26) Klug, H.; Alexander, l. *X-ray Diffraction Procedures for Polycrystalline and Amorphous Materials*, 2nd ed.; John Wiley and Sons: New York, 1974.
(27) Langford, I.; Louër, D. *Rep. Prog, Phys.* **1996**, *59*, 131.
(28) Balzar, D.; Ledbetter, H. *J. Appl. Crystallogr*. **1993**, *26*, 97.
(29) Langford, J. *J. Appl. Crystallogr*. **1978**, *11*, 10.
(30) Delhez, R.; De Keijser, T.; Mittemeijer, E. *Fresenius Z. Anal. Chem.* **1982**, *312*, 1.
(31) Cheary, R.; Coelho, A. *X-ray Line Profile Fitting Program, XFIT*; School of Physical Sciences, University of Technology: Sydney, Australia.
(32) Cheary, R.; Coelho, A. *J. Appl. Crystallogr*. **1998**, *31*, 851.
(33) Alexander, L. *J. Appl. Phys*. **1954**, *25*, 155.
(34) *Diffrac^{plus} TOPAS*, version 2.0; Advanced X-ray Solutions Software: Bruker, Germany.
(35) Cheary, R.; Coelho, A. *J. Appl. Crystallogr*. **1992**, *25*, 109.
(36) Milev, A.; Kannangara, G. S. K.; Wilson, M. *Langmuir* **2004**, *20*, 1888.
(37) Milev, A.; Kannangara, G. S. K.; Ben-Nissan, B.; Wilson, M. *J. Phys. Chem. B* **2004**, *108*, 5516.
(38) Milev, A.; Kannangara, G. S. K.; Ben-Nissan, B. *Mater. Lett.* **2003**, *57*, 1960.
(39) Featherstne, J.; Pearson, S.; LeGeros, R. *Caries Res.* **1984**, *18*, 63.
(40) Laugier, J.; Bochu, B. (Développé au Laboratoire des Matériaux et du Génie Physique Ecole Nationale Supérieure de Physique de Grenoble).
(41) Barralet, J.; Best, S.; Bonfield, W. *J. Biomed. Mater. Res.* **1998**, *41*, 79.
(42) Arends, J.; Davidson, C. *Calcif. Tissue Res.* **1975**, *18*, 65.
(43) LeGeros, R.; Trautz, O.; Klein, E.; LeGeros, J. *Experientia* **1969**, *25*, 5.
(44) Elliott, J.; Holcomb, D.; Young, R. *Calcif. Tissue Int.* **1985**, *37*, 372.
(45) Daculsi, G.; LeGeros, R, *J. Dent. Res.* **1986**, *65*, 802.
(46) Termine, J.; Lundy, D. *Calcif. Tissue Res.* **1973**, *13*, 73.
(47) Magne, D.; Pilet, P.; Weiss, P.; Daculsi, G. *Bone* **2001**, *29*, 547.
(48) LeGeros, R.; Trautz, O.; LeGeros, J.; Klein, E. *Bull. Soc. Chim. Fr*. **1968**, 1712.
(49) LeGeros, R.; LeGeros, J.; Trautz, O.; Shirra, W. *Adv. X-ray Anal*. **1971**, *14*, 57.
(50) Rogers, K.; Daniels, P. *Biomaterials* **2002**, *23*, 2577.
(51) Handschin, S.; Stern, W. *Bone* **1995**, *16*, 355.
(52) Lundey, D.; Eanes, E. *Archs. Oral Biol*. **1973**, *18*, 813.
(53) Finean, J.; Engstrom, A. *Biochim. Biophys. Acta* **1953**, *13*, 183.